Invited Articles

Dimensionless parameters for cloudy Rayleigh-Bénard convection: Supersaturation, Damköhler, and Nusselt numbers

Subin Thomas [1], Prasanth Prabhakaran [1], Fan Yang [2]
Will H. Cantrell [1], and Raymond A. Shaw [1,*]
[1]*Department of Physics, Michigan Technological University, Houghton, Michigan 49931, USA*
[2]*Brookhaven National Laboratory, Upton, New York 11973, USA*

(Received 29 July 2021; accepted 3 January 2022; published 27 January 2022)

In steady-state Rayleigh-Bénard convection, heat is transported by turbulent thermal convection from the bottom, hot surface to the top, cold surface, leading to a height-independent sensible heat flux. When water vapor is present and cloud formation occurs, there is also an additional latent heat flux. Heat transport in cloudy Rayleigh-Bénard convection depends on turbulent flow as well as the microphysical state of the clouds: specifically, whether substantial supersaturations exist and whether cloud liquid water is removed through sedimentation/precipitation. In this article we bridge between the Rayleigh-Bénard convection literature and the atmospheric literature. We express the governing equations for cloudy convection in dimensionless form, thereby explicitly identifying the governing parameters relevant to the cloudy case, including Schmidt, Damköhler, supersaturation, and sedimentation numbers. We further connect to the atmospheric literature by obtaining a Nusselt number (dimensionless heat flux) for a cloud-convection system, directly from the conservation equations for temperature and water vapor. This flux has the same form as that identified by Zhang *et al.* [L. Zhang, K. L. Chong, and K.-Q. Xia, J. Fluid Mech. **874**, 1041 (2019)] for convection with water vapor, but is extended to the cloudy case. For equal thermal and water vapor diffusivities, the flux corresponds to the widely used atmospheric quantities equivalent temperature and moist static energy. Using large eddy simulation (LES) of an idealized cloudy Rayleigh-Bénard convection system with fixed boundary conditions, we find that the equivalent heat flux (Nusselt number) is only weakly dependent on the microphysical details of the system, such as liquid water mixing ratio and cloud droplet number concentration. From the results, we show the vertical profiles of sensible and latent heat fluxes depend on the liquid water content, whereas the equivalent heat flux remains a constant throughout the height of the chamber.

DOI: 10.1103/PhysRevFluids.7.010503

I. INTRODUCTION

Classical Rayleigh-Bénard convection is described by the Rayleigh number, $\mathrm{Ra} = g\beta\Delta T H^3/(\nu_T \nu)$, which captures the competing roles of buoyancy forcing and diffusive losses, and the Prandtl number, $\mathrm{Pr} = \nu/\nu_T$, which is a material parameter defining the relative magnitude of diffusion of momentum and thermal energy. Here, g is the magnitude of gravitational acceleration, β is the coefficient of thermal expansion, ν_T is the thermal diffusivity, ν is the kinematic viscosity, and H is the vertical separation between surfaces with imposed temperature difference ΔT. For sufficiently large Ra, and $\mathrm{Pr} \sim 1$, relevant to atmospheric flows, the convecting flow is strongly

*rashaw@mtu.edu

turbulent. The hallmark of turbulent convection, in turn, is efficient transport of energy. The nondimensional heat flux is given by the Nusselt number Nu, the ratio of the total heat flux to the conductive heat flux ($\nu_T \Delta T/H$) across an identical, static fluid layer:

$$\mathrm{Nu} = \frac{\overline{w'T'} + \nu_T \nabla_z \overline{T}}{\nu_T \Delta T/H}, \tag{1}$$

where w is the vertical component of velocity, the overbar denotes ensemble average over a horizontal surface, and the prime denotes fluctuations from the mean [1]. By definition, in steady state this horizontally averaged heat flux is constant with height within the convecting fluid. Seeking an understanding of the Nusselt number and its dependence on the Rayleigh number remains a challenge even for single-fluid ("dry") convection [1,2]. When phase changes are included at the boundaries, even in idealized laboratory convection experiments, the heat flux problem becomes much more complex [3]. Furthermore, the flux problem becomes complex in the presence of phase change effects in the bulk as it introduces an additional heat source/sink via latent heat associated with the phase change processes [4,5]. Additionally, the amount of condensate in the system depends on the rate at which phase change effects (e.g., condensation/evaporation) occur. In the context of cloudy convection, the rate of evaporation/condensation is strongly influenced by the properties of the aerosols and cloud droplets including size, number concentration, etc. (henceforth, referred to as "microphysics"). For example, if the condensate load is fixed, plentiful small droplets allow for efficient conversion of water vapor to the condensed phase compared to a few large droplets. Additionally, small droplets have lower sedimentation velocities and thus result in a higher condensate load in the system [5].

The idealization of Rayleigh-Bénard convection has a long history in guiding our understanding of cloud formation [6–11]. In the atmospheric context the conundrum posed by the interaction between temperature, water vapor, and liquid water on large scales is circumvented by using conserved variables derived from thermodynamics. In this work, however, we consider cloud formation in traditional, laboratory-scale Rayleigh-Bénard convection as a model problem for mixing clouds. At the same time, the fluid dynamics community has explored the parameter space for moist Rayleigh-Bénard convection in the absence of any liquid water [3]. In Sec. II, we present the governing equations for cloudy Rayleigh-Bénard convection and introduce and discuss the associated dimensionless parameters. Then in Sec. III we provide a nonthermodynamic derivation of an equivalent heat flux weakly dependent on the microphysics of the system and subsequently a Nusselt number independent of any cloud droplets analogous to and thus expanding the scope of the Nusselt number proposed by Zhang *et al.* [3]. Furthermore, under the assumptions of constant molecular/turbulent diffusivities of temperature and water vapor, we retrieve the equivalent temperature and moist static energy from the flux derivations that are widely used in the atmospheric sciences community (see Sec. III). Both of those are derived using only the first law and therefore avoid problems of reversibility [12,13]. It should be noted that the equivalent temperature flux is not limited to atmospheric applications but can be extended to systems with phase change and chemically reactive systems (see Sec. VI).

In this article we aim to connect the Rayleigh-Bénard literature with the atmospheric science literature in two ways. We present the equations for cloudy convection in dimensionless form, making clear the relevant parameters describing the system. It is a curiosity of cloud physics that the governing equations are rarely stated in dimensionless form. Building on some of the efforts that have already been made in that direction [14–19] we carefully identify all relevant dimensionless quantities for cloudy Rayleigh-Bénard convection. As part of that, and as described in the previous paragraph, we derive an equivalent Nusselt number for cloudy Rayleigh-Bénard convection, directly from the equations for temperature and water vapor mixing ratio. Entropy conservation is not assumed in the derivation and thus nonequilibrium conditions can be adequately represented; nevertheless, the derived heat flux is constant with height throughout the convection system, independent of the dimensionless parameters related to the microphysical properties of

the cloud. We present large eddy simulations (LES) of cloudy Rayleigh-Bénard convection with varying aerosol conditions to explore and illustrate the characteristics and the utility of the approach. Specifically, we use aerosol injection rate as a way to explore the dependence of dimensionless parameters describing the cloud microphysics (e.g., Damköhler number and sedimentation or Rouse number) and the heat flux (Nusselt number) at constant Rayleigh number. In the final section, we discuss the prospective implications of the conserved flux and its applications, as well as its connections to atmospheric variables.

II. GOVERNING EQUATIONS AND DIMENSIONLESS PARAMETERS FOR CLOUDY CONVECTION

A. Governing equations in dimensional form

The momentum equation for cloudy Rayleigh-Bénard convection can be written as (Kumar *et al.* [20])

$$\frac{\partial \mathbf{U}}{\partial t} + \mathbf{U}\cdot\boldsymbol{\nabla}\mathbf{U} = -\frac{1}{\rho_a}\boldsymbol{\nabla} p + [\beta(T-\overline{T}) + \epsilon(Q_v - \overline{Q_v}) - Q_L]g\hat{z} + \nu\nabla^2\mathbf{U}, \tag{2}$$

where $\mathbf{U}$ is the velocity vector, ρ_a is the density of air, p is the pressure, and ν is the kinematic viscosity. The buoyancy term contains three contributions multiplied by the gravitational acceleration g, which acts in the vertical $\hat{z}$ direction. First, the contribution from the difference between the temperature T of the fluid parcel and the average value $\overline{T}$, multiplied by the thermal expansion coefficient β. Second, a contribution from the density difference of water vapor expressed in terms of mixing ratio Q_v (the ratio of the mass of water vapor to the mass of the dry air) multiplied by the term $\epsilon = m_d/m_v - 1$, where m_d and m_v are the molecular weights of dry air and water vapor, respectively. Third, a contribution of the condensed liquid water expressed again in terms of mixing ratio Q_L, which accounts for the drag force applied to the fluid due to settling cloud droplets.

For Rayleigh-Bénard convection with phase change effects, the continuity equation, the energy equation, and the water vapor and liquid mass balance equations can be written as

$$\frac{D\rho}{Dt} + \rho\boldsymbol{\nabla}\cdot\mathbf{U} = 0, \tag{3}$$

$$\frac{\partial T}{\partial t} = \boldsymbol{\nabla}\cdot(-\mathbf{U}T + \nu_T\boldsymbol{\nabla}T) + \frac{L_v}{C_p}\dot{Q}_L, \tag{4}$$

$$\frac{\partial Q_v}{\partial t} = \boldsymbol{\nabla}\cdot(-\mathbf{U}Q_v + \nu_v\boldsymbol{\nabla}Q_v) - \dot{Q}_L, \tag{5}$$

$$\frac{\partial Q_L}{\partial t} = \boldsymbol{\nabla}\cdot(-\mathbf{U}Q_L + w_T Q_L\hat{z}) + \dot{Q}_L, \tag{6}$$

where $\rho = \rho_a(1 + 0.61Q_v - Q_L)$, ν_T and ν_v are thermal and water vapor diffusivities, respectively, C_p is the specific heat at constant pressure, L_v is the latent heat of vaporization of water, w_T is the terminal speed of a cloud droplet, and $\dot{Q}_L$ is the rate of condensation/evaporation of water. It should be noted here that, while we include the sedimentation term in Eq. (6), we have not included a corresponding energy-loss term in Eq. (4) because the thermal inertia of droplets is negligible for typical cloud conditions.

B. Nondimensional formulation

It is instructive to consider the nondimensional form of the governing equations. We take the height of the chamber (H) and the free-fall velocity for dry Rayleigh-Bénard convection ($w = \sqrt{g\beta\Delta T H}$) as the scales for length and velocity. The nondimensional scaled variables (denoted by the tilde on top of the variable) of length, time, velocity, temperature, and water vapor for moist Rayleigh-Bénard convection are $\tilde{L} = L/H$, $\tilde{t} = tw/H$, $\tilde{\mathbf{U}} = \mathbf{U}/w$, $\tilde{T} = \frac{T-\overline{T}}{\Delta T}$, and $\tilde{Q}_v = \frac{Q_v - \overline{Q_v}}{\Delta Q_v}$.

The acceleration due to gravity is g, thermal expansion coefficient is β, ϵ is the ratio of dry air to water vapor gas constants, and ΔT and ΔQ_v are the temperature and water vapor mixing ratio differences between the bottom and top plates, respectively. Using these scales, the nondimensional momentum equation is written as

$$\frac{\partial \tilde{\mathbf{U}}}{\partial \tilde{t}} + \tilde{\mathbf{U}} \cdot \tilde{\boldsymbol{\nabla}} \tilde{\mathbf{U}} = -\frac{1}{\rho_a} \tilde{\boldsymbol{\nabla}} \tilde{p} + (\tilde{T} + B_v \tilde{Q}_v - B_L)\hat{z} + \sqrt{\frac{\mathrm{Pr}}{\mathrm{Ra}}} \tilde{\boldsymbol{\nabla}}^2 \tilde{\mathbf{U}}, \tag{7}$$

where Ra is the Rayleigh number ($\mathrm{Ra} = \frac{g\beta \Delta T H^3}{\nu_T \nu}$) and Pr is the Prandtl number ($\mathrm{Pr} = \nu/\nu_T$). The second term grouped within brackets on the right side of Eq. (7) is the buoyancy contribution to momentum, and acts along the direction of gravity. Again, the buoyancy contribution comes from temperature, water vapor, and the drag associated with the sedimentation of the condensate. The dimensionless parameter for water vapor is $B_v = \epsilon \Delta Q_v/(\beta \Delta T)$ and that for liquid water is $B_L = Q_L/(\beta \Delta T)$.

The dimensionless equation for temperature [Eq. (4)] can be rewritten as follows:

$$\frac{\partial \tilde{T}}{\partial \tilde{t}} + \tilde{\mathbf{U}} \cdot \tilde{\boldsymbol{\nabla}} \tilde{T} = \frac{1}{\sqrt{\mathrm{Ra}\,\mathrm{Pr}}} \tilde{\nabla}^2 \tilde{T} + \frac{L_v}{C_p \Delta T} \frac{H}{w} \frac{Q_L}{\tau_c}. \tag{8}$$

Here, we have taken $\dot{Q}_L = Q_L/\tau_c$, where τ_c is a characteristic time for the condensation process. We then note that the terms $L_v/(C_p \Delta T)$ and τ_t/τ_c, where $\tau_t = H/w$, are dimensionless numbers associated with the cloud condensation process. The timescale for condensation can be conceptually understood by considering the idealization of growth of a population of single-sized cloud droplets in a supersaturated environment. The growth rate of a cloud of droplets with number density N and radius R is

$$\dot{Q}_L = \frac{\rho_l}{\rho_a} \frac{d}{dt} \left(\frac{4\pi}{3} N R^3 \right) = \frac{\rho_l}{\rho_a} 4\pi N R^2 \frac{dR}{dt}, \tag{9}$$

where ρ_l is the density of water and ρ_a is the density of air. Using an expression for the droplet growth rate $d\overline{R}/dt$, Eq. (9) can be written as [21]

$$\dot{Q}_L = 4\pi \xi N R \bar{s} \frac{\rho_l}{\rho_a}. \tag{10}$$

Here $s = p_v/p_s - 1$ is the water vapor supersaturation (the excess water vapor pressure compared to the saturation vapor pressure). The factor ξ is associated with diffusion of water vapor to a growing droplet, and the associated heat conduction away from the droplet due to latent heat release during the droplet growth [21]. Thus, the phase relaxation time (τ_c) can be understood as the timescale at which droplets respond to any change in its surrounding environment, defined as $\tau_c = (4\pi \xi N \overline{R})^{-1}$ [22]. Assuming the flux timescale, given by $\tau_t = H/w$, represents the scales at which environment changes, the Damköhler number (Da) can be defined as τ_t/τ_c [15]. At very high Damköhler numbers, the droplets respond quickly to any change in the surrounding environment and conversely at small Damköhler numbers the environment changes faster than the droplets can respond to it. Hence, these regimes are called fast and slow microphysics, respectively. Therefore, Eq. (8) can be rewritten as

$$\frac{\partial \tilde{T}}{\partial \tilde{t}} + \tilde{\mathbf{U}} \cdot \tilde{\boldsymbol{\nabla}} \tilde{T} = \frac{1}{\sqrt{\mathrm{Ra}\,\mathrm{Pr}}} \tilde{\nabla}^2 \tilde{T} + \frac{1}{\mathrm{Ste}} \frac{\rho_l}{\rho_a} \mathrm{Da}\, \bar{s}. \tag{11}$$

We note that the expression on the right-hand side consists of dimensionless quantities $\mathrm{Ste} = C_p \Delta T/L_v$, ρ_l/ρ_a, Da, and $\bar{s}$, where Ste is the Stefan number. Similarly, the equation for the water vapor mixing ratio becomes

$$\frac{\partial \tilde{Q}_v}{\partial \tilde{t}} + \tilde{\mathbf{U}} \cdot \tilde{\boldsymbol{\nabla}} \tilde{Q}_v = \frac{1}{\sqrt{\mathrm{Ra}\,\mathrm{Sc}\,\mathrm{Le}}} \tilde{\nabla}^2 \tilde{Q}_v - \frac{1}{\Delta Q_v} \frac{\rho_l}{\rho_a} \mathrm{Da}\, \bar{s}, \tag{12}$$

TABLE I. Dimensionless parameters for the microphysical state in cloudy Rayleigh-Bénard convection.

Dimensionless parameter	Definition	Description
Ra	$g\beta\Delta T H^3/(\nu_T \nu)$	Buoyancy forcing and diffusive losses
B_v	$\epsilon \Delta Q_v/(\beta \Delta T)$	Relative contribution of water vapor to buoyancy
B_L	$Q_L/(\beta \Delta T)$	Relative contribution of cloud water to buoyancy
Pr	ν/ν_T	Diffusion of momentum relative to thermal energy
Sc	ν/ν_v	Diffusion of momentum relative to water vapor
Le	ν_T/ν_v	Diffusion of thermal energy relative to water vapor
Da	τ_t/τ_c	Rate of water vapor condensation in a cloud relative to rate of turbulent mixing
s	$Q_v/Q_s(T) - 1$	Excess water vapor driving condensation
Ste	$C_p \Delta T/L_v$	Latent heat compared to sensible heat
Rou	w_t/w	Rate of removal of cloud droplets by sedimentation relative to rate of turbulent mixing
Nu_μ	Eq. (22)	Equivalent energy flux relative to conductive flux

where Sc is the Schmidt number ($\mathrm{Sc} = \nu/\nu_v$) and Le is the Lewis number ($\mathrm{Le} = \mathrm{Sc}/\mathrm{Pr}$). Using $\tilde{Q}_L = Q_L/\Delta Q_v$, the nondimensional form of liquid water mixing ratio [Eq. (6)] is

$$\frac{\partial \tilde{Q}_L}{\partial \tilde{t}} + \tilde{\mathbf{U}} \cdot \tilde{\nabla} \tilde{Q}_L = \mathrm{Rou}\, \tilde{\nabla} \tilde{Q}_L \hat{z} + \frac{1}{\Delta Q_v} \frac{\rho_l}{\rho_a} \mathrm{Da}\, \bar{s}. \tag{13}$$

An additional dimensionless group appears, the ratio of the droplet terminal speed and the convection free-fall speed, which is sometimes referred to as the Rouse number $\mathrm{Rou} = w_T/w$ [23,24]. It is essentially a gravitational settling parameter or, it can be expressed as the inverse of a dimensionless droplet residence time $\tau_t/\tau_{\mathrm{res}}$.

The dimensionless parameters appearing in these equations are summarized in Table I. The parameters Pr, Sc, and Le describe material properties, so for a water-air system as in Earth clouds, they are essentially constants. Furthermore, for saturated boundaries and a given mean temperature, the quantity ΔQ_v can be related to ΔT by the Clausius-Clapeyron equation $d \ln p_s/dT = L_v/(RT^2)$, where p_s is the saturation water vapor pressure. Therefore, B_v can be interpreted as a material property for given mean temperature and boundary conditions. It should be noted, however, that if the assumption of saturated boundaries is relaxed, then B_v becomes an independently determined quantity; for example, consider experiments in which the lower boundary contains a salt solution and therefore has reduced vapor pressure [25]. The Stefan number Ste represents the relative significance of sensible and latent heat effects due to phase changes; for plausible values of ΔT, water clouds always satisfy $\mathrm{Ste} \ll 1$. The dimensionless parameters that describe the cloud microphysical properties are s, Da, Rou, and B_L. It can be noted that B_L connects the microphysics directly to the buoyancy term in the Navier-Stokes equation, but in fact the phase changes described by s and Da also influence the buoyancy term through their contributions to the T and Q_v fields. Finally, the state of macroscopic convection is described by the dimensionless parameter Ra, as well as a Nusselt number Nu discussed in the next section.

III. HEAT FLUX AND AN EQUIVALENT NUSSELT NUMBER

A defining aspect of convection is the efficient transfer of energy, which can be expressed through the dimensionless Nusselt number. Here we outline a simple route to obtaining a Nusselt number for cloudy convection and discuss its relationship to known variables of atmospheric thermodynamics and the relevance of cloud microphysical properties. We proceed initially with the dimensional forms of the equations for notational clarity.

Applying Reynolds decomposition, we write the instantaneous variable as a sum of the mean and the fluctuations represented by the overbar and prime, respectively,

$$U = \overline{U_i} + u_i'; \quad T = \overline{T} + T'; \quad Q_v = \overline{Q_v} + Q_v', \tag{14}$$

and it then follows from Eqs. (4) and (5) that the mean scalar evolution equations are

$$\frac{\partial \overline{T}}{\partial t} = \boldsymbol{\nabla} \cdot (-\overline{U_i T} - \overline{u_i' T'} + \nu_T \boldsymbol{\nabla} \overline{T}) + \frac{L_v}{C_p} \overline{\dot{Q}_L}, \tag{15}$$

$$\frac{\partial \overline{Q_v}}{\partial t} = \boldsymbol{\nabla} \cdot (-\overline{U_i Q_v} - \overline{u_i' Q_v'} + \nu_v \boldsymbol{\nabla} \overline{Q_v}) - \overline{\dot{Q}_L}. \tag{16}$$

The two scalar equations can be combined together by eliminating the net condensation/evaporation rate $\overline{\dot{Q}_L}$ by adding Eq. (15) and $L_v/C_p \times$ Eq. (16):

$$\frac{\partial}{\partial t}\left(\overline{T} + \frac{L_v}{C_p}\overline{Q_v}\right) = \boldsymbol{\nabla} \cdot \left[-\overline{U_i}\left(\overline{T} + \frac{L_v}{C_p}\overline{Q_v}\right) - \overline{u_i'\left(T' + \frac{L_v}{C_p}Q_v'\right)}\right] + \boldsymbol{\nabla} \cdot \boldsymbol{\nabla}\left(\nu_T \overline{T} + \nu_v \frac{L_v}{C_p}\overline{Q_v}\right). \tag{17}$$

Equation (17), steady in time and averaged over a plane with normal along the direction of gravity, is

$$\nabla_z \cdot (-\overline{w'T'} + \nu_T \nabla_z \overline{T}) + \frac{L_v}{C_p} \nabla_z \cdot (-\overline{w'Q_v'} + \nu_v \nabla_z \overline{Q_v}) = 0. \tag{18}$$

Please note, the mean advection of temperature in the vertical direction, $\overline{WT}$, is zero, since $\overline{W} = 0$ from the continuity equation for the Rayleigh-Bénard convection of Chillà and Schumacher [1]. From Eq. (18), a constant surface flux is obtained along the z direction:

$$\Phi_\mu = \overline{w'T'} + \frac{L_v}{C_p}\overline{w'Q_v'} - \nu_T \nabla_z \overline{T} - \frac{L_v}{C_p}\nu_v \nabla_z \overline{Q_v}. \tag{19}$$

Thus, an effective Nusselt number can be defined as

$$\mathrm{Nu}_\mu = \frac{\overline{w'T'} + \frac{L_v}{C_p}\overline{w'Q_v'} - \nu_T \nabla_z \overline{T} - \frac{L_v}{C_p}\nu_v \nabla_z \overline{Q_v}}{\nu_T \frac{\Delta T}{H} + \nu_v \frac{L_v}{C_p}\frac{\Delta Q_v}{H}}. \tag{20}$$

This flux [Eq. (19)] has been obtained from the temperature and water vapor equations, and has no explicit dependence on the rate and amount of condensation or evaporation occurring within the flow. It depends only on the temperature difference and water vapor difference imposed at the top and bottom boundaries across the convecting system. This flux, referred to as equivalent temperature flux, remains a constant throughout the height of the chamber. It is therefore internally independent of any microphysical variations within the convection, for example due to gravitational settling or height-dependent condensation rate. Any change in Φ_μ or Nu_μ due to a change in mean-microphysics properties must come through the density of the fluid and the covariance terms $\overline{w'T'}$ and $\overline{w'Q_v'}$. Although it cannot be shown theoretically that this flux is the same for all possible microphysical conditions, the LES studies presented in the next section indicate that the flux in Eq. (19) does not vary significantly with the condensation rate profile, and also appears to be independent of the cloud microphysics in the bulk. We note that Eq. (20) is identical to the Nusselt number obtained by Zhang *et al.* [3] for moist convection without phase change; here we have demonstrated that it is identical for cases with phase change effects as well.

In fact, assuming temperature and water vapor to have the same diffusivities, the Nusselt number can be written solely in terms of the familiar atmospheric quantity "equivalent temperature" (e.g., refer to Eq. 6.74, p. 285 of Bohren and Albrecht [13]):

$$T_e = T + (L_v/C_p)Q_v. \tag{21}$$

The equivalent temperature is defined as the temperature a moist air parcel would have if all its water vapor were to condense in an adiabatic, isobaric process. Such a process is allowed by the first law of thermodynamics, but is prohibited by the second law of thermodynamics for a closed system [13]. This connection is discussed further in Sec. VI.

Following the same steps but using the dimensionless forms of the governing equations, we get the flux [Eq. (19)] in terms of non-dimensional quantities.

$$\tilde{\Phi}_\mu = \overline{\tilde{W}\cdot\left(\tilde{T}+\frac{L_v}{C_p}\frac{\Delta Q_v}{\Delta T}\tilde{Q}_v\right)} - \frac{1}{\sqrt{\mathrm{Ra}}}\left(\frac{1}{\sqrt{\mathrm{Pr}}}\tilde{\boldsymbol{\nabla}}\tilde{T}+\frac{L_v}{C_p}\frac{\Delta Q_v}{\Delta T}\frac{1}{\sqrt{\mathrm{Sc\,Le}}}\tilde{\boldsymbol{\nabla}}\tilde{Q}_v\right)_z \tag{22}$$

The Nusselt number expressed in terms of other nondimensional numbers is

$$\mathrm{Nu}_\mu = \frac{\Phi_\mu}{\frac{L_v}{C_p}\frac{\Delta Q_v}{\Delta T}\frac{1}{\sqrt{\mathrm{Ra\,Sc\,Le}}}\Delta\tilde{Q}_v+\frac{1}{\sqrt{\mathrm{Ra\,Pr}}}\Delta\tilde{T}}, \tag{23}$$

$$\mathrm{Nu}_\mu = \frac{\overline{\tilde{W}\cdot\left(\tilde{T}+\frac{L_v}{C_p}\frac{\Delta Q_v}{\Delta T}\tilde{Q}_v\right)}}{\frac{L_v}{C_p}\frac{\Delta Q_v}{\Delta T}\frac{1}{\sqrt{\mathrm{Ra\,Sc\,Le}}}\Delta\tilde{Q}_v+\frac{1}{\sqrt{\mathrm{Ra\,Pr}}}\Delta\tilde{T}} - \frac{\frac{1}{\sqrt{\mathrm{Ra}}}\left(\frac{1}{\sqrt{\mathrm{Pr}}}\tilde{\boldsymbol{\nabla}}\tilde{T}+\frac{L_v}{C_p}\frac{\Delta Q_v}{\Delta T}\frac{1}{\sqrt{\mathrm{Sc\,Le}}}\tilde{\boldsymbol{\nabla}}\tilde{Q}_v\right)_z}{\frac{L_v}{C_p}\frac{\Delta Q_v}{\Delta T}\frac{1}{\sqrt{\mathrm{Ra\,Sc\,Le}}}\Delta\tilde{Q}_v+\frac{1}{\sqrt{\mathrm{Ra\,Pr}}}\Delta\tilde{T}} - 1. \tag{24}$$

From Eqs. (22) and (23), we note that the flux has no explicit dependence on Damköhler number and supersaturation, the two microphysically relevant dimensionless parameters. As discussed above, however, the microphysics can affect the Nusselt number through density of the fluid, and through the magnitude of covariance terms. The possible dependence on microphysics is further explored in the next section. Compared to the dry-convection Nusselt number, which depends only on Ra and Pr, for cloudy convection the dimensionless parameters Sc and Le are also needed.

IV. NUMERICAL SIMULATIONS OF MOIST RAYLEIGH-BÉNARD CONVECTION WITH VARYING CLOUD MICROPHYSICS

In this section, we explore the equivalent temperature flux and the equivalent temperature derived in Sec. III by simulating moist Rayleigh-Bénard convection under varying microphysical conditions. The simulations are motivated by prior observations from and simulations of the Pi convection-cloud chamber [4,5,15]. The convection is initiated by imposing an unstable gradient of temperature and water vapor between the top and bottom plates. The bottom and top plates are maintained at saturated conditions at 290 and 276 K, respectively. The sidewalls have adiabatic conditions for both temperature and water vapor mixing ratio, and a no-slip/no-penetration condition for velocity. The different aerosol injection rates used in the current study are listed in Table II, with a cloud-free case included for reference. They are selected so as to achieve Damköhler numbers varying by a factor of approximately 20, centered on $\mathrm{Da}\sim 1$, thereby allowing both "fast" and "slow" microphysics regimes to be explored [15]. Corresponding steady-state microphysical properties including the liquid water mixing ratio, the cloud droplet number concentration, mean diameter, and water vapor supersaturation are also listed in Table II. As the aerosol injection rate is increased, the cloud droplet number concentration increases and the mean diameter decreases. For the $\mathrm{Da}>1$ cases, we also note that the mean supersaturation is quite small, so aerosol activation by fluctuations likely becomes the dominant source of cloud droplets [26]. Finally, we also observe an increase in the liquid water content as the aerosol injection rate is increased, because smaller cloud droplets have lower sedimentation rates. The result is a monotonic increase in total water content, which has implications for the effective temperature in the system (discussed later).

Details of the model setup for the Pi convection-cloud chamber are discussed by Thomas *et al.* [5]. A brief description of the model is provided here for the sake of completeness. The simulations use the modified System for Atmospheric Modeling (SAM) [27] combined with a spectral bin microphysics (SBM) algorithm [28]. The SAM is a LES code that solves the equations of motion under the anelastic approximation, and that uses a Smagorinsky model for the subgrid scales. The equations are integrated using a third-order Adams-Bashforth scheme on a fully staggered Arakawa

TABLE II. Varying microphysical conditions explored in the simulations of moist Rayleigh-Bénard convection. The table shows aerosol (cloud condensation nucleus) injection rate, liquid water mixing ratio, total water (vapor plus liquid) mixing ratio, cloud droplet number concentration, mean cloud droplet radius, mean supersaturation, Rouse (sedimentation) number, and Damköhler number. Injection rate is the number of particles per grid volume (linear dimension 3.125 cm) per model time step (0.02 s). The simulations span a factor of ∼20 in Da, centered on Da ∼ 1.

Reference	Injection rate (s^{-1})	Q_L (g/kg)	Q_T (g/kg)	N (cm^{-3})	$\bar{R}$ (μm)	s (%)	Rou	Da
A	0.005	0.09	8.22	22.0	7.9	1.26	0.87	0.19
B	0.006	0.11	8.24	37.6	7.2	0.82	0.55	0.30
C	0.007	0.12	8.25	46.6	6.8	0.69	0.55	0.35
D	0.008	0.13	8.26	56.6	6.6	0.58	0.55	0.41
E	0.009	0.14	8.27	67.5	6.3	0.50	0.55	0.47
F	0.01	0.20	8.37	225.8	4.8	0.16	0.35	1.2
G	0.02	0.25	8.45	493.2	4.0	0.08	0.22	2.1
H	0.03	0.29	8.51	909.3	3.3	0.06	0.14	3.3
I	0.05	0.32	8.56	1541.2	2.8	0.05	0.09	4.6
J	0.0	0.0	8.53	0.0	0.0	10.48		

C-type grid with uniform horizontal and vertical grid sizes. The prognostic scalars are advected using a multidimensional positive definite advection transport algorithm [29]. Boundary fluxes are calculated using Monin-Obukhov similarity theory (MOST).

A SBM algorithm based on Chen and Lamb [28] is implemented in SAM to simulate aerosol-cloud interactions. In this study, monodisperse aerosol particles are injected uniformly in the chamber at a constant rate. Once aerosol particles take up water to become haze (unactivated droplets with radii smaller than 1 μm) and cloud (droplets with radii larger than 1 μm) droplets, we use 40 mass-doubling bins starting from 0.1 μm to represent the droplet size distribution. One advantage of this SBM algorithm is that it resolves several crucial microphysical processes such as deliquescence of dry aerosol and condensational growth of haze and cloud droplets, including solute and curvature effects (see details in Sec. 3 in [28]), thereby allowing proper representation of the activation process. The present study focuses only on warm clouds with droplet activation and diffusional growth, and the effects of collisional growth is turned off.

We consider a convection chamber of dimensions 2 m × 2 m × 1 m along the x, y, and z directions, respectively, motivated by the geometry of the Pi chamber [5]. The computational domain is discretized uniformly with cubic boxes of side length 3.125 cm yielding 64 × 64 × 32 grid boxes. The time step is 0.02 s, and the system is initialized with an unstable temperature and water vapor gradient. For the current study, we allow the system to evolve in a cloud-free state and reach a steady supersaturation of 10.48%. Monodisperse salt particles with a radius of 62.5 nm are injected uniformly in the volume of the chamber at a constant rate. Dry aerosols become haze droplets if the environmental saturation ratio is larger than the specified deliquescent relative humidity (set to be 75%). The cloud reaches a steady state after about an hour of simulated time when activation of cloud droplets due to condensational growth of haze droplets is balanced by the removal of cloud droplets due to sedimentation. On reaching a steady state with respect to microphysics after 1 h, the system is allowed to evolve for another 2 h (for comparison, the free-fall time is of order 1 s and the large-scale circulation time is of order 1 min).

After 1 h of physical time, three-dimensional (3D) fields are output every 5 min for the next 2 h to obtain statistically independent droplet size distributions within the simulated cloud chamber (this time is chosen so as to be larger than the large-scale circulation time so as to ensure independence). Each grid point thus has a cloud droplet number concentration sorted into 33 different bins according to their sizes. The fluxes are evaluated from 3D fields of velocity u, v, w, temperature, water vapor, and liquid water mixing ratio.

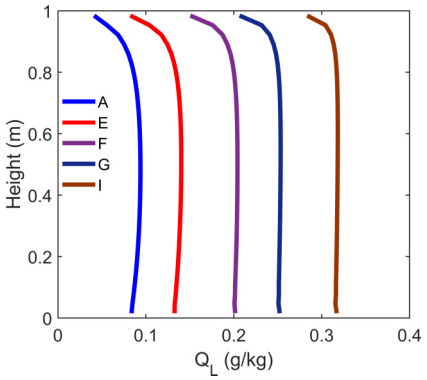

FIG. 1. Vertical profiles of liquid water mixing ratio for five of the cases. These profiles were obtained by horizontal averaging of the 3D output obtained every 5 min within a span of 2 h, after reaching a steady state. The colors refer to different CCN injection rates (for details refer to Table II).

V. RESULTS: LES OF CLOUDY CONVECTION WITH VARYING MICROPHYSICS

A. Vertical profiles of scalars

The injection of aerosols into the supersaturated system described in Sec. IV results in the formation of cloud droplets. The liquid water content in the chamber reaches a steady state through a dynamic equilibrium between condensational growth and gravitational sedimentation. As shown already in Table II, and as observed in both experiments and prior simulations [5,15], increasing the aerosol injection rate results in a corresponding increase in the steady-state liquid water content in the cloudy Rayleigh-Bénard convection system. Vertical profiles of liquid water mixing ratio for five of the cases are shown in Fig. 1, further demonstrating that mean Q_L increases with increasing aerosol injection rate. More significantly, they show a nontrivial spatial variability, emphasizing the significance of the internal microphysics independence of the equivalent temperature flux Φ_μ.

Figure 2 shows vertical profiles of temporally and horizontally averaged temperature, water vapor mixing ratio, and equivalent temperature [Eq. (21)] for the different aerosol injection rates. As stated in Eq. (10), the condensation rate is proportional to $\overline{NRs}$, where N is the number concentration of droplets and $\overline{R}$ is the mean droplet radius, and therefore generally increases with aerosol injection

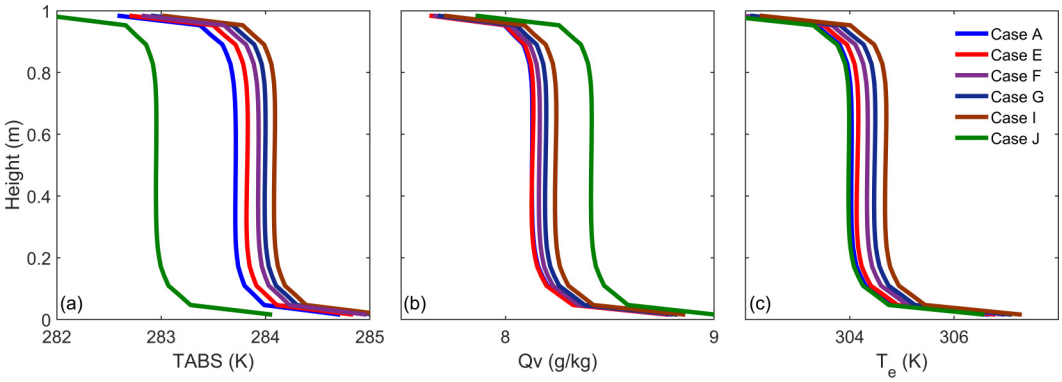

FIG. 2. Averaged profiles of (a) temperature, (b) water vapor mixing ratio, and (c) equivalent temperature [Eq. (21)]. These profiles were obtained by horizontal averaging of the 3D output obtained every 5 min within a span of 2 h, after reaching a steady state. The colors refer to different CCN injection rates (for details refer to Table II).

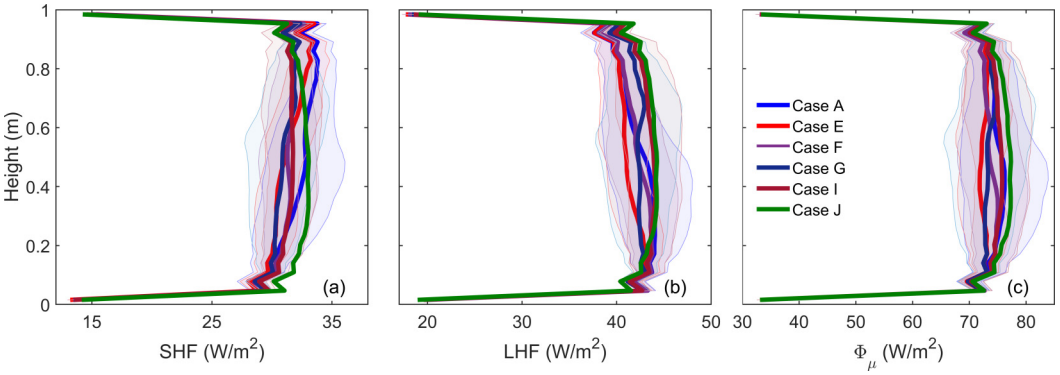

FIG. 3. Time-averaged profiles of (a) sensible heat flux ($\rho C_p \overline{w'T'}$), (b) latent heat flux ($\rho L_v \overline{w'Q_v'}$), and (c) equivalent temperature flux Φ_μ, as defined in Eq. (19), from 3D outputs sampled at a frequency of 5 min for 2 h. The shaded region shows the turbulent variability in the data. The line colors refer to the different CCN injection rates, as defined in Table II.

rate (cf. Table II). That leads to an increase in the bulk temperature due to the enthalpy change associated with condensation (latent heat), as shown in Fig. 2(a). The mean water vapor mixing ratio, shown in Fig. 2(b), is reduced from the zero-aerosol case denoted by the green line. In spite of the net decrease from the zero-aerosol case, Q_v increases monotonically with increasing aerosol injection rate, which is a direct result of the increasing temperature in the bulk, given that the humidity is always close to 100%. Taken together, the reduction in the mean water vapor mixing ratio and the increase in the mean temperature result in a much lower supersaturation for cloudy conditions compared to moist conditions without any aerosols. Therefore, as evident from Table II, the mean bulk supersaturation shifts towards zero as the number concentration and liquid water content increase. We observe a monotonic increase of equivalent temperature in Fig. 2(c) with increasing cloud droplet number concentration. From a parcel point of view, i.e., for a closed system, one would expect the equivalent temperature to be a constant for a given total water content. However, the system is not closed and the total water content inside the cloud chamber is not necessarily a constant for different aerosol injection rates. As the number of cloud droplets increases, the droplet radius decreases, thereby increasing the droplet lifetime. Thus, with a reduced precipitation efficiency, the total water content, and consequently the equivalent temperature, increases (cf. Table II).

B. Sensible heat flux, latent heat flux, and equivalent temperature flux

The sensible heat flux (SHF), latent heat flux (LHF), and equivalent temperature flux defined in Eq. (19) are plotted in Fig. 3. The boundary flux contributions are discussed later, and only the turbulent fluxes are considered in this figure. In the bulk, the turbulent transport terms for scalars are of the form $\overline{u_i'\phi'}$, where ϕ' is the fluctuation component of a scalar. The turbulent sensible heat flux and latent heat flux at any height z are given by

$$\mathrm{SHF}_{\mathrm{turbulent}} = \rho_z C_p \overline{u_z' T'}, \tag{25}$$

$$\mathrm{LHF}_{\mathrm{turbulent}} = \rho_z L_v \overline{u_z' Q_v'}. \tag{26}$$

The height-dependent density ρ_z has to be multiplied to account for non–Oberbeck-Boussinesq effects associated with strong temperature gradients. Again, the subgrid-scale fluxes and boundary contributions are not considered here, therefore these equations alone are applied along the height of the chamber to generate Fig. 3. As mentioned in Sec. IV the boundary fluxes are parametrized using MOST; such parametrizations are used in atmospheric models due to insufficient resolution of the grids close to the walls. The MOST parameters have been tuned to simulate a convective cloud

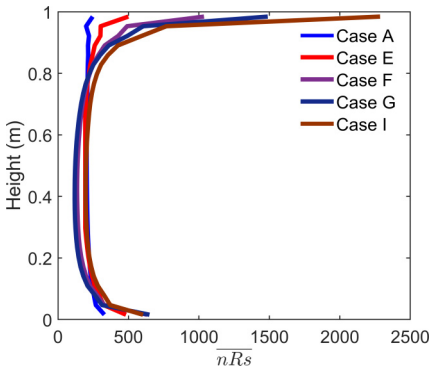

FIG. 4. Averaged profile of $\overline{nRs}$. These profiles were obtained by horizontal averaging of the 3D output obtained every 5 min within a span of 2 h, after reaching a steady state. The colors refer to different CCN injection rates (for details refer to Table II).

chamber in Thomas *et al.* [5]. The effects of these parametrizations are confined to the boundaries, and hence are not plotted in Fig. 3 and leave some residual fluctuations. Further, the focus of the current study is the bulk flow, where the turbulent fluxes are more significant than the diffusive fluxes. Hence, for consistency we have plotted the horizontally averaged vertical profile of $\rho_z C_p \overline{w'T'}$ for SHF and $\rho_z L_v \overline{w'Q_v'}$ for LHF in Fig. 3.

The variability inherent in the turbulent flow is shown with shading, obtained from the standard deviation of the average values of 12 samples, with each sample representing a 10-min average (roughly ten large-scale circulation times). It can be considered the uncertainty in the flux profiles, given the finite sample time. The averaged equivalent temperature flux, as predicted, remains constant within turbulent variability compared to SHF and LHF under different aerosol injection rates. Specifically, the sensible and latent heat flux profiles for cases A, B, C, D, and E are strongly sloped, and the curves lie outside the uncertainty envelopes near the top and bottom boundaries (not all curves are shown, for the sake of clarity). The equivalent temperature fluxes calculated for different aerosol injection rates, however, fall within the inherent turbulent variability.

The profiles of SHF [Fig. 3(a)] and LHF [Fig. 3(b)] can be interpreted by considering the governing equations for temperature and water vapor in the presence of cloud droplets, Eqs. (4) and (5). For a steady-state system the left sides of Eqs. (4) and (5) are zero. On applying Reynolds decomposition and horizontal area averaging, the first term in $C_p \times$ Eq. (4) is the sensible heat flux $C_p(\overline{u_z'T'} - \nu_T \nabla_z \overline{T})$, and the first term in $L_v \times$ Eq. (5) is the latent heat flux $L_v(\overline{u_z'Q_v'} - \nu_v \nabla_z \overline{Q_v})$. Under these assumptions, $C_p \times$ Eq. (4) and $L_v \times$ Eq. (5) can be written as

$$\frac{d(\overline{\mathrm{SHF}})}{dz} = L_v \overline{\dot{Q}_L}, \tag{27}$$

$$\frac{d(\overline{\mathrm{LHF}})}{dz} = -L_v \overline{\dot{Q}_L}. \tag{28}$$

From Eqs. (27) and (28) it is clear that a net condensation rate results in vertical gradients of SHF and LHF, and that horizontally averaged vertical profiles of SHF and LHF have opposite slopes for the low cloud droplet number cases A–E with Da < 1, as illustrated in Fig. 3 (not all shown, for the sake of clarity). Figure 4 shows vertical profiles of $\overline{nRs}$ as a proxy for condensation rate. This illustrates the low- and high-Da regimes, in which the condensation rate is distributed throughout the volume versus the condensation rate being stronger near the boundaries. We see that though the condensation rates for cases A and I are identical in the bulk, near the top and bottom boundaries they vary substantially. For a high Da number such as case I, any supersaturation is consumed by the presence of the large concentration of cloud droplets. Hence, any supersaturation variation occurs

only close to the boundaries. Further, the nonlinear behavior of number concentration, radius of the droplets, and supersaturation (e.g., see Chandrakar *et al.* [15] and [30]) between low Da and high Da causes the LHF and SHF to behave nonlinearly with Da. However, as the number of cloud droplets in the bulk increases, the supersaturation approaches water vapor saturation (see Table II). In such cases, any supersaturation is produced at the boundaries due to the mixing of plumes from the boundary with the bulk parcels thus localizing condensation predominantly to the boundaries. Therefore, the slope of SHF and LHF in the bulk of the chamber, characterizing the condensation rate, reduces as shown by the SHF and LHF profiles of cases F–I with Da > 1, illustrated in Fig. 3 (again, not all profiles are shown, for clarity). As noted previously, from the derivation we expect the equivalent temperature flux Φ_μ to remain a constant along the height of the chamber. Panel (c) of Fig. 3 demonstrates that, indeed, Φ_μ remains within the turbulent variability for different cloud droplet number cases.

VI. DISCUSSION

The theoretical analysis and LES results presented so far confirm that the equivalent temperature flux Φ_μ in cloudy convection is constant within the convection flow, and therefore can serve as the basis for defining a Nusselt number. The LES results further suggest that, at least for the conditions investigated, it is only weakly dependent on the microphysical details and the resulting rate of condensation/evaporation in the fluid. Additionally, the theoretical analysis implies that Φ_μ is independent of the nature of the cloud droplet formation: heterogeneous (aided by aerosols, as in the current study) or homogeneous, e.g., [31]. Indeed, Φ_μ is only a function of Ra, Pr, Sc, and Le. The fact that this equivalent temperature flux is independent of the form of phase change aids in generalizing the present work to any form of phase change in the bulk. This would indicate that a convective system with a heat source/sink in the core of the flow, similar to effects of a first-order phase transition, will have an equivalent temperature flux similar to the one in Eq. (19).

As an example, we consider the simple case of a boiling system [32]. A similar formulation is applicable in the context of a two-phase boiling convection system (e.g., boiling of water), where the roles of vapor and liquid are reversed with reference to the current study. The sign of the phase change term in the temperature, water vapor, and liquid water equation is reversed. Furthermore, the rate of boiling in the bulk of the fluid will depend on the number concentration of the bubbles and their total surface area, similar to the observations discussed in Sec. V. Thus, the net heat flux in a boiling convective system will have the exact form as Eq. (19), assuming the latent heat of condensation and the latent heat of vaporization are identical.

Additionally, this analysis can be extended to chemically reacting systems, where the heat release/absorption associated with the reaction is analogous to the latent heat of condensation/evaporation in a cloudy system. Indeed, the Damköhler number discussed in the present work is borrowed from studies involving chemically reacting systems, and is used for identifying slow, moderate, and fast reaction with respect to the flow timescale [33]. Thus, a chemically reacting system is analogous to a cloudy convection system, and will have an equivalent temperature flux that will be independent of the Damköhler number. This is typically accomplished by using an enthalpy-based treatment.

The discussion so far suggests that in a convection system, the heat released/absorbed in the bulk of the fluid due to phase change effects or chemical reactions does not influence internal changes in the equivalent temperature flux, which only depends on the boundary contributions. Thus, this flux is conserved and could be used for identifying the effects of nonconservative contributions to the flow, such as entrainment effects in a cloudy boundary layer flow (see the next paragraph on atmospheric implications for additional details) and evaporating jets. Additionally, the properties of the equivalent temperature flux are applicable in the context of extrasolar planetary atmospheres that have cloud systems composed of fluids with properties very different from that of water [31,34].

The current work has several connections to the atmospheric thermodynamics literature. Equation (17) reduces to an advection-diffusion equation for the equivalent temperature T_e given by

Eq. (21) when the molecular diffusivities of temperature and water vapor are identical. As typically derived, equivalent temperature (e.g., Eq. 6.74 of Albrecht and Bohren [13]) does not require isentropic assumptions, and hence can represent nonequilibrium conditions such as those illustrated in the previous section. Additionally, the equivalent temperature has an adiabatic definition that can be connected to the equivalent potential temperature. The corresponding derivation, however, assumes saturated conditions, which limits its utility for conditions far from equilibrium. Replacing Q_s with Q_v,

$$\theta_e = \theta \exp(L_v Q_v / C_p T) \approx \theta + L_v Q_v / C_p. \tag{29}$$

The second equality is not an approximation when defining the first-law version of the equivalent temperature [21]. Finally, multiplying the second equality in Eq. (29) with C_p, gives another familiar atmospheric quantity, the moist static energy $S_e = C_p T + gz + L_v Q_v$. The moist static energy is obtained from the first law and is essentially equivalent to the enthalpy [35]. It has been widely used to study the energy budget in deep convective clouds as well as the response of clouds to entrainment [36–39].

VII. SUMMARY AND OUTLOOK

In an effort to help in connecting the fluid dynamics and cloud physics literature, we began this article by nondimensionalizing the governing equations for cloudy Rayleigh-Bénard convection. Specifically, the equations of temperature and water vapor mixing ratio include terms related to the rate of condensation, which is tied to the microphysical properties of the cloud, such as droplet number concentration and mean radius. Traditional dry Rayleigh-Bénard convection can be described by the Rayleigh number and the Prandtl number. When cloud formation is included, the dimensionless space becomes vastly more complex. We identify the additional dimensionless parameters of the Damköhler number, Rouse number (also known as the settling parameter), Stefan number, Schmidt number, and Lewis number as relevant for cloudy Rayleigh-Bénard convection. Dimensionless terms that related to the relative contributions of water vapor (B_v) and condensed cloud (B_L) water to the buoyancy are also identified.

In Sec. III, we have derived a flux Φ_μ that is independent of microphysical details, and should therefore remain a constant throughout the height of a convection-cloud chamber. Subsequently, we use this flux to expand the definition of Nusselt number to include the effect of cloud condensation. It turns out to be identical to the Nusselt number proposed by Zhang *et al.* [3] for cloud-free convection. We show that Φ_μ and the resulting Nusselt number can be related to the equivalent temperature, as well as to the moist static energy, commonly used in atmospheric thermodynamics.

In Sec. V we demonstrate that the equivalent temperature flux is nearly constant for different aerosol injection cases using an atmospheric LES modified to simulate cloudy Rayleigh-Bénard convection. One of the caveats associated with atmospheric models is that they assume the same turbulent diffusivities for temperature and water vapor. We demonstrate the increase in latent heat flux and a commensurate decrease in the sensible heat flux with height from the bottom surface, as a result of the volumetric heating due to condensation. Further, we demonstrate that these profiles of latent heat flux and sensible heat flux within the chamber change as a function of the condensation rate within the bulk of the chamber, depending on the Damköhler number.

In Sec. VI, we point out that the nondimensionalization presented here may lend itself to application in cloudy convection in other contexts, such as extrasolar planetary atmospheres. Furthermore, we explore the possibility of using fluxes analogous to the equivalent temperature flux for other phase change systems such as boiling convection systems and for chemically reacting systems. Ideally, investigations using particle-resolved direct numerical simulations would allow for a more detailed investigation of the behavior of the equivalent temperature flux. Thus a parameter space varying Ra, Pr, Sc, and Da can be explored from a fluid dynamics perspective and from an atmospheric context. Further aspects can also be explored, for example the effect of roughness and surface flux parametrizations.

ACKNOWLEDGMENTS

This work was supported by NSF Grant No. AGS-1754244 and Department of Energy Grant No. DE-SC0012704. Portage, a high-performance computing infrastructure at Michigan Technological University, was used in obtaining the results presented in this article. We are grateful to Mikhail Ovchinnikov for help implementing SAM.

[1] F. Chillà and J. Schumacher, New perspectives in turbulent Rayleigh-Bénard convection, Eur. Phys. J. E **35**, 58 (2012).

[2] K. P. Iyer, J. D. Scheel, J. Schumacher, and K. R. Sreenivasan, Classical 1/3 scaling of convection holds up to Ra = 10^{15}, Proc. Natl. Acad. Sci. USA **117**, 7594 (2020).

[3] L. Zhang, K. L. Chong, and K.-Q. Xia, Moisture transfer by turbulent natural convection, J. Fluid Mech. **874**, 1041 (2019).

[4] D. Niedermeier, K. Chang, W. Cantrell, K. K. Chandrakar, D. Ciochetto, and R. A. Shaw, Observation of a link between energy dissipation rate and oscillation frequency of the large-scale circulation in dry and moist Rayleigh-Bénard turbulence, Phys. Rev. Fluids **3**, 083501 (2018).

[5] S. Thomas, M. Ovchinnikov, F. Yang, D. van der Voort, W. Cantrell, S. K. Krueger, and R. A. Shaw, Scaling of an atmospheric model to simulate turbulence and cloud microphysics in the Pi chamber, J. Adv. Model. Earth Syst. **11**, 1981 (2019).

[6] R. Krishnamurti, On cellular cloud patterns. Part 1: Mathematical model, J. Atmos. Sci. **32**, 1353 (1975).

[7] J. W. Deardorff, Stratocumulus-capped mixed layers derived from a three-dimensional model, Boundary-Layer Meteorol. **18**, 495 (1980).

[8] C. S. Bretherton, A theory for nonprecipitating moist convection between two parallel plates. Part I: Thermodynamics and "linear" solutions, J. Atmos. Sci. **44**, 1809 (1987).

[9] C.-H. Moeng and R. Rotunno, Vertical-velocity skewness in the buoyancy-driven boundary layer, J. Atmos. Sci. **47**, 1149 (1990).

[10] O. Pauluis and J. Schumacher, Self-aggregation of clouds in conditionally unstable moist convection, Proc. Natl. Acad. Sci. USA **108**, 12623 (2011).

[11] G. K. Vallis, D. J. Parker, and S. M. Tobias, A simple system for moist convection: The Rainy–Bénard model, J. Fluid Mech. **862**, 162 (2019).

[12] K. A. Emanuel, *Atmospheric Convection* (Oxford University Press, New York, 1994).

[13] C. F. Bohren and B. A. Albrecht, Atmospheric Thermodynamics (Oxford University Press, New York, 2000).

[14] C. A. Jeffery, Inhomogeneous cloud evaporation, invariance, and Damköhler number, J. Geophys. Res. **112**, D24S21(2007).

[15] K. K. Chandrakar, W. Cantrell, K. Chang, D. Ciochetto, D. Niedermeier, M. Ovchinnikov, R. A. Shaw, and F. Yang, Aerosol indirect effect from turbulence-induced broadening of cloud-droplet size distributions, Proc. Natl. Acad. Sci. USA **113**, 14243 (2016).

[16] M. Pinsky, A. Khain, and A. Korolev, Theoretical analysis of mixing in liquid clouds–Part 3: Inhomogeneous mixing, Atmos. Chem. Phys. **16**, 9273 (2016).

[17] C. Siewert, J. Bec, and G. Krstulovic, Statistical steady state in turbulent droplet condensation, J. Fluid Mech. **810**, 254 (2017).

[18] M. Pinsky and A. Khain, Theoretical analysis of mixing in liquid clouds—Part IV: DSD evolution and mixing diagrams, Atmos. Chem. Phys. **18**, 3659 (2018).

[19] J. Fries, G. Sardina, G. Svensson, and B. Mehlig, Key parameters for droplet evaporation and mixing at the cloud edge, Q. J. R. Meteorol. Soc. **147**, 2160 (2021).

[20] B. Kumar, J. Schumacher, and R. A. Shaw, Cloud microphysical effects of turbulent mixing and entrainment, Theor. Comput. Fluid Dyn. **27**, 361 (2013).

[21] M. K. Yau and R. R. Rogers, *A Short Course in Cloud Physics* (Elsevier, New York, 1996).

[22] A. Kostinski, Simple approximations for condensational growth, Environ. Res. Lett. **4**, 015005 (2009).

[23] L. Freire, M. Chamecki, and J. Gillies, Flux-profile relationship for dust concentration in the stratified atmospheric surface layer, Boundary-Layer Meteorol. **160**, 249 (2016).
[24] D. Richter and M. Chamecki, Inertial effects on the vertical transport of suspended particles in a turbulent boundary layer, Boundary-Layer Meteorol. **167**, 235 (2018).
[25] A. S. M. Shawon, P. Prabhakaran, G. Kinney, R. A. Shaw, and W. Cantrell, Dependence of aerosol-droplet partitioning on turbulence in a laboratory cloud, Geophys. Res. Atmos. **126**, e2020JD033799 (2021).
[26] P. Prabhakaran, A. S. M. Shawon, G. Kinney, S. Thomas, W. Cantrell, and R. A. Shaw, The role of turbulent fluctuations in aerosol activation and cloud formation, Proc. Natl. Acad. Sci. USA **117**, 16831 (2020).
[27] M. F. Khairoutdinov and D. A. Randall, Cloud resolving modeling of the arm summer 1997 IOP: Model formulation, results, uncertainties, and sensitivities, J. Atmos. Sci. **60**, 607 (2003).
[28] J.-P. Chen and D. Lamb, Simulation of cloud microphysical and chemical processes using a multicomponent framework. Part I: Description of the microphysical model, J. Atmos. Sci. **51**, 2613 (1994).
[29] P. K. Smolarkiewicz and W. W. Grabowski, The multidimensional positive definite advection transport algorithm: Nonoscillatory option, J. Comput. Phys. **86**, 355 (1990).
[30] K. K. Chandrakar, W. Cantrell, and R. A. Shaw, Influence of turbulent fluctuations on cloud droplet size dispersion and aerosol indirect effects, J. Atmos. Sci. **75**, 3191 (2018).
[31] P. Prabhakaran, S. Weiss, A. Krekhov, A. Pumir, and E. Bodenschatz, Can Hail and Rain Nucleate Cloud Droplets?, Phys. Rev. Lett. **119**, 128701 (2017).
[32] J.-Q. Zhong, D. Funfschilling, and G. Ahlers, Enhanced Heat Transport by Turbulent Two-Phase Rayleigh-Bénard Convection, Phys. Rev. Lett. **102**, 124501 (2009).
[33] M. J. Molemaker and J. V.-G. de Arellano, Control of chemical reactions by convective turbulence in the boundary layer, J. Atmos. Sci. **55**, 568 (1998).
[34] C. Helling, Exoplanet clouds, Annu. Rev. Earth Planet. Sci. **47**, 583 (2019).
[35] J.-I. Yano and M. H. Ambaum, Moist static energy: Definition, reference constants, a conservation law and effects on buoyancy, Q. J. R. Meteorol. Soc. **143**, 2727 (2017).
[36] H. Riehl and J. S. Malkus, On the heat balance in the equatorial trough zone, Geophysica **6**, 503 (1958).
[37] M. Yanai, S. Esbensen, and J.-H. Chu, Determination of bulk properties of tropical cloud clusters from large-scale heat and moisture budgets, J. Atmos. Sci. **30**, 611 (1973).
[38] T. Yamaguchi and D. A. Randall, Cooling of entrained parcels in a large-eddy simulation, J. Atmos. Sci. **69**, 1118 (2012).
[39] J. P. Mellado, Cloud-top entrainment in stratocumulus clouds, Annu. Rev. Fluid Mech. **49**, 145 (2017).